Calculation of Transonic Flows with Separation Past Arbitrary Inlets at Incidence

Arvin Shmilovich*
Aerodynamics Research and Technology, Douglas Aircraft Company, Long Beach, California

A method of calculating transonic separated flows past arbitrary inlets at incidence and yaw is presented. The inviscid flow solver is based on the transonic potential equation, which is approximated and solved numerically on a boundary-conforming coordinate system. The multrigrid finite-volume method is used to solve the flow equation. The inviscid flow technique is coupled with an interactive boundary-layer method that uses an inverse formulation to calculate shock-induced separated flows. Experimental results obtained for several nacelle configurations are used to evaluate the accuracy of the method in predicting flowfields for a wide range of operational conditions.

Introduction

IT is of practical interest to develop an efficient method of calculating flowfields past general three-dimensional inlet configurations. The concern of the designer is primarily centered around several important features associated with the flow phenomena in the transonic flow regime: the shock location, its strength, its impact on the boundary layer, and the magnitude of the pressure peak at the lip. Obviously, a refined engineering design that does not suffer excessive drag and degradation of engine performance has to benefit from the analysis of these flow characteristics.

Several computational methods for calculating inlet flowfields have been developed. Arlinger[1] and Caughey and Jameson[2] used the analytical transformation of the potential equation into a body-fitted mesh system to compute the inviscid flow past axisymmetric inlets at zero incidence. Three-dimensional flows about arbitrary inlets at angle of attack were computed by Reyhner[3] who used the full potential formulation on stretched cylindrical coordinates. The equation is solved sequentially on radial grid surfaces, all of which pass through the nacelle centerline. The H-type nonbody-fitted grids are wasteful in distributing the mesh points in the farfield regions, and they require extrapolation to enforce the no-flux boundary conditions on the nacelle surface. A finite-difference scheme for solving the potential equation on three-dimensional body-conforming grids was developed by Chen and Caughey.[4] This method is restricted to axisymmetric geometries only. Although the grids were oriented with the body surfaces, the procedure uses special operators to enforce the no-flow condition across the solid boundaries.

Euler and Navier-Stokes algorithms have also been developed for the calculation of inlet flowfields. References 5 and 6 describe methods for analyzing axisymmetric inlets at zero incidence. The method developed by Vadyak[7] is for the analysis of general three-dimensional inlet flowfields. This reference presents solutions obtained for very mild flow conditions at which the flow is separated.

The main theme in the present study is to develop a computational tool for predicting transonic viscous flows about inlets with reasonable expenditure of computer resources. Emphasis is placed upon the ability to simulate separated flows. In response to the need for analyzing general nacelle configurations at arbitrary incidence, a finite-volume method for the potential equation originally devised by Jameson and Caughey[8] is employed. This method uses surface-oriented C-type grids generated by Halsey.[9] To enhance the practicality of three-dimensional inlet calculations on fine meshes, the multigrid technique[10-12] is utilized to speed up convergence to small residuals.

The inviscid flow module is coupled with a finite-difference interactive boundary-layer method in order to simulate viscous effects. There are various inverse methods that can be used to include viscous effects. The technique developed by Cebeci[13] and Cebeci et al.[14] is used in this study to calculate shock-induced separated flows. Either a displacement thickness or a surface-blowing technique can be used to simulate the viscous effects, both methods producing almost identical solutions. Results show that the interactive procedure is very efficient, usually requiring up to ten boundary-layer updates for large separation bubbles.

Experimental results obtained for several nacelle configurations were used to evaluate the accuracy of the method in predicting flowfields for a wide range of operational conditions, i.e., high and low mass flow ratios for subsonic, transonic, and mild supersonic freestream Mach numbers. Slotted wind-tunnel wall boundary conditions were implemented to account for discrepancies between experimental data and free-air calculations for nearly sonic freestream velocities. These are of importance for this speed regime, since supersonic pockets extend close to the walls and wall interference can no longer be ignored.

In the following sections the multigrid finite-volume method is described, emphasizing aspects of computations for inlet geometries. The boundary-layer technique is reviewed to lay the groundwork for understanding the features associated with the interface procedure used for coupling the viscous and inviscid flowfields. Calculations demonstrating the capability of the method to simulate complex shock/boundary-layer interactive flows are presented. The emphasis in the flow results is laid heavily upon the study of separated flows, and the validity of the numerical prediction is confirmed for a variety of flow conditions.

Analysis

Inviscid Flow

The continuity equation in Cartesian coordinates is

$$(\rho u)_x + (\rho v)_y + (\rho w)_z = 0 \tag{1}$$

Presented as Paper 88-0707 at the AIAA 26th Aerospace Sciences Meeting, Reno, NV, Jan. 11-14, 1988; received May 7, 1988; revision received Nov. 15, 1988.

*Senior Engineer/Scientist. Member AIAA.

where u v and w are the components of the velocity vector in the x, y and z directions, respectively. The density ρ is related to the magnitude of the velocity vector via the isentropic relation. The description of the velocity $\bar{q} = (u, v, w)$ in terms of a scalar potential $\bar{q} = \nabla\phi$ is adequate on the premise that there are no strong shocks contained in the flowfield. Under the transformation to an arbitrary coordinate system X,Y,Z, the conservation law is cast in the form

$$(\rho hU + P)_X + (\rho hV + Q)_Y + (\rho hW + R)_Z = 0 \qquad (2)$$

where h denotes the Jacobian of the transformation and (U,V,W) is the contravariant velocity vector. Here, P, Q and R are fluxes representing the artificial viscosity,[11] which is introduced in hyperbolic regions of the flowfield to remove the symmetry of the central-difference formulas used in the subsonic region. These fluxes are constructed such that the second-order accuracy is maintained at nearly all supersonic points yet supplies enough viscosity in high-gradient regions to stabilize the computation for strong shocks.

Bilinear variations for the coordinates and the potential are used for the local transformation of each mesh cell into a cube in the computational domain. Thus, the discretized form of the conservative law, Eq (2), becomes

$$\mu_{YZ}\delta_X(\rho hU + P) + \mu_{ZX}\delta_Y(\rho hV + Q) + \mu_{XY}\delta_Z(\rho hW + R) = 0 \qquad (3)$$

where μ and δ are center averaging and differencing operators, respectively.

The contravariant fluxes are calculated using difference formulas for the derivatives of the transformation at the center of the mesh cells. In subsonic regions the differencing scheme [Eq. (3)] can be interpreted as conserving mass fluxes in an auxiliary cell that overlaps eight primary cells and has its vertices at the centers of the primary cells. Thus, a mass flux balance may be carried out in the auxiliary cell associated with each mesh point using the coordinates and the potential at that point and those of its 26 neighbors.

Figure 1 presents the grid distribution on the inlet surface, the fan face, and one of the radial planes that form the three-dimensional grid system. The topology of the mesh system at the axis is different from any other region in the domain. A grid point on the axis is common to more than eight mesh cells (depending upon the number of radial planes used in the calculation). Also, the cells whose edges form the inlet axis are of triangular shape in the cross-sectional planes. The finite-volume formulation cannot be applied on the axis, and the complication is circumvented by utilizing the potential equation in Cartesian coordinates.

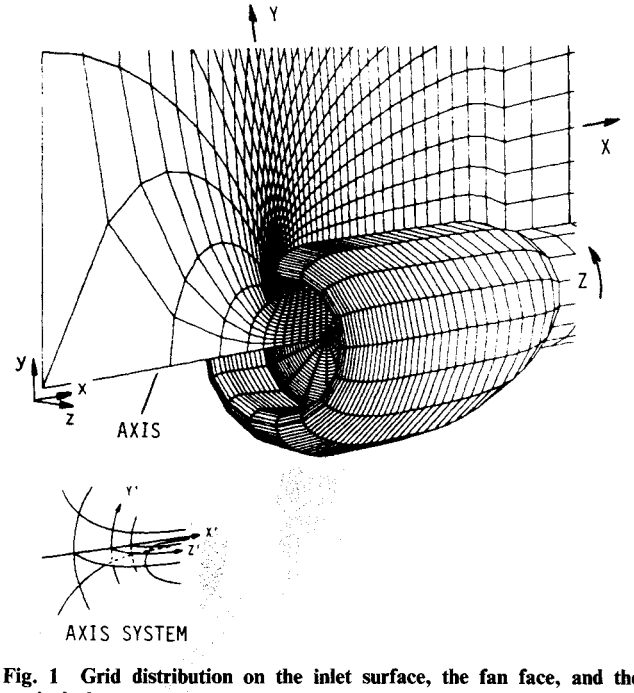

Fig. 1 Grid distribution on the inlet surface, the fan face, and the vertical plane.

Using the relationships between the derivatives of the potential function in physical coordinates and its derivatives in a local arbitrary coordinate system X',Y',Z' (see Ref. 15), the potential equation can be expressed as

$$d_1\phi_{X'X'} + d_2\phi_{Y'Y'} + d_3\phi_{Z'Z'} + d_4\phi_{X'Y'} + d_5\phi_{Y'Z'} + d_6\phi_{X'Z'} + e_1\phi_{X'} + e_2\phi_{Y'} + e_3\phi_{Z'} = 0 \qquad (4)$$

The system is schematically defined in the inset in Fig. 1 in which the intersection region between the vertical and the nearly horizontal planes is shown. The tridiagonal system resulting from the discretization of Eq. (4) is inverted after each fine grid iteration to update the potential on the axis.

Boundary Conditions

The advantage of implementing the finite-volume technique within a body-fitted grid system is the ease with which boundary conditions can be enforced. Across the inlet surfaces, the no-flux condition $\partial\phi/\partial n = 0$ is incorporated by reflecting the normal contravariant flux contribution for the cells adjacent to the boundary. The no-flux condition is also applied on the sting upon which the inlet is assumed to be mounted in the numerical simulation. This condition is adequate even for flow-through inlets or inlets having exhaust jets since it was experimentally found that the conditions of variable jets do not appreciably affect the inlet pressure aside from the immediate vicinity of the exhaust (see Ref. 16). The no-flux condition is removed when the blowing velocity approach is used for the viscous/inviscid interaction. This will be discussed in a subsequent section.

To remove the singularity of the potential at infinity, a reduced velocity potential G representing perturbations from the freestream is introduced. For a freestream with angle of attack α and yaw angle β, G is related to the potential ϕ by

$$\phi = G + x\cos\alpha\cos\beta + y\sin\alpha\cos\beta + z\sin\beta \qquad (5)$$

On the upstream and lateral farfield boundaries of the computational domain, the reduced potential is set to zero. At the far downstream boundary, the flow is assumed to be fully developed, and the first derivative in the freestream direction of the perturbation potential is set to zero. The Neumann condition for the potential is incorporated into the multigrid process by introducing fictitious cells next to the downstream boundary. The velocities in the streamwise direction at the center of these cells are adjusted so that they have the required value on the boundary.

Inside the nacelle at the fan face, the flow is also assumed to be fully developed with a uniform velocity in the axial direction $(1 + k)$ the freestream velocity. The potential at points on this boundary is calculated by applying the procedure used at the downstream boundary. The parameter

$$k = \frac{A_{hl}}{A_{ff}} \cdot MFR\left[1 - \frac{\gamma - 1}{2} M_\infty^2 k(k+2)\right]^{-1/\gamma - 1} - 1 \qquad (6)$$

is obtained by using isentropic relations, and it is related to the engine power setting via the mass flux ratio. The freestream Mach number is M_∞, and γ is the ratio of specific heats. A_{hl} is the highlight area of the nacelle defined by the leading-edge radius, and A_{ff} is the inlet cross-sectional area at the fan face. The mass flux ratio is defined by $MFR = A_o/A_{hl}$ where A_o is the capture area defined by the stagnation streamtube far upstream.

Homogeneous slotted wind-tunnel wall boundary conditions are simulated according to[17]

$$\phi_x + F \cdot \frac{HTD}{2} \phi_{xy} = 0 \tag{7}$$

where HTD is the height to inlet diameter ratio and F is the slot parameter related to the geometrical arrangement of the slots. On integration along the wall in the axial direction, this boundary condition reads

$$A\phi_X + \phi_Y + B\phi = 0 \tag{8}$$

where the coefficients are related to F, HTD, and derivatives of the transformation. The discretization formula

$$A\phi_{i-1,j} + (3 + 2B)\phi_{i,j} + A\phi_{i+1,j} = 4\phi_{i,j+1} - \phi_{i,j+2} \tag{9}$$

is inverted after each fine-grid sweep to update the potential at points on the wall. Here, ϕ_X is approximated with a two-point central-difference formula and ϕ_Y is replaced by a three-point backward difference. The index j represents the grid line that defines the wall, and $j+1$ and $j+2$ designate the wrapping-around grid lines next to it. The x component of velocity far downstream is readjusted after every wall-boundary update to account for the mass flux across the walls. This mode of discretization has proven stable for the range of parameters used in the calculations.

Multigrid Iterative Process

Noting that the equation representing conservation of mass is analogous to the potential equation in quasilinear form, the latter is utilized for formulating the iterative scheme. The iterative technique to solve the algebraic equations resulting from the discretization is interpreted as a time-stepping method to an artificial time-dependent process. To be effective with the multigrid technique, the relaxation scheme must effectively damp the high wave-number components of the residual. Ordinarily, iterative procedures are local in nature and therefore quite suitable for this purpose. One such process is characterized by considering one mesh line at a time and simultaneously calculating the corrections at points that lie on it. This line-overrelaxation is performed successively until the solution in the entire domain is updated. The system of equations to be solved on each line is a pentadiagonal, diagonally dominant system.

The system of equations for the XSLOR scheme, i.e., when the corrections are simultaneously calculated along X-lines, is sequentially solved on planes of constant Z and is of the form

$$a_1 C_{i,j-2,k} + a_2 C_{i,j-1,k} + a_3 C_{i,j,k} + a_4 C_{i,j+1,k}$$
$$a_5 C_{i-2,j,k} + a_6 C_{i-1,j,k} + a_7 C_{i,j,k-1} = -R_{i,j,k} \tag{10}$$

for positive components of the contravariant velocity. Here, $C_{i,j,k}$ is the correction to be computed at point (i, j, k) and $R_{i,j,k}$ is the residual calculated [by Eq. (3)] using values of the solution from the previous iteration.

In a similar fashion it is possible to devise a scheme in which points along Y lines are updated simultaneously, marching in the Y direction (YSLOR). Both X and Y schemes are used in an alternate mode within each multigrid cycle.

Viscous Flow

A succinct description of the boundary-layer problem and the strategy used for the viscous calculation is presented here. The conventional method for solving the boundary-layer equations subject to a prescribed pressure distribution has been proven useful for many applications. However, in situations where the flowfields contain regions of separation, the direct formulation exhibits a singularity that hinders the numerical calculation. The singularity is removed by reformulating the problem so that the boundary-layer equations are solved in an inverse mode in which the external flowfield is computed as part of the solution.

With the assumptions that the flow is nearly aligned with the longitudinal grid lines and that the displacement thickness is small relative to the inlet radius, the inverse procedure in the present work uses the first-order boundary-layer equations for two-dimensional laminar and turbulent flows. The eddy viscosity formulation of Cebeci and Smith[18] is used for the turbulence model. The relationship

$$u_e^v(s) = \frac{1}{\pi} \int_{s_a}^{s_b} \frac{1}{\rho_e} \frac{d}{d\xi} (\rho_e u_e \delta^*) \frac{d\xi}{s - \xi} \tag{11}$$

determines the perturbation velocity $u_e^v(s)$ due to the displacement thickness δ^* in a region bounded by s_a and s_b. The velocity at the edge of the boundary layer $u_e(s)$ is the sum of the inviscid velocity $u_e^i(s)$ and the viscous perturbation velocity,

$$u_e(s) = u_e^i(s) + u_e^v(s) \tag{12}$$

and it provides an outer boundary condition for the compressible boundary-layer flow problem. For transonic flows with shocks, this is regarded as an empirical equation that provides a relationship between external velocity and displacement thickness. The discretization employs the second-order box scheme developed by Keller,[19] which proved to be efficient and reliable for various viscous flow problems. The marching technique used in the numerical procedure is stabilized in regions of recirculating flow using the FLARE approximation,[20] which assumes that the convective term in the streamwise direction is negligible. An extensive discussion on the aspects of computation of the boundary-layer equations may be found in Refs. 13, 14, and 19.

Viscous-Inviscid Interaction

An interface procedure is incorporated to provide the necessary link between the inviscid and viscous solutions in an interactive mode. The coupling plays a pivotal role, and it must be carefully devised so that instability is not incurred during the calculation process. Two approaches have been considered for the coupling process. In the displacement thickness approach, gradients in flow properties are neglected in the inviscid flow domain bounded by the edge of the displacement thickness and the edge of the boundary layer. The inviscid flow solver can be readily used if the no-flux condition is applied at the edge of the displacement thickness. If the convenience of using the flux reflection for enforcing this condition is still sought, a new body-fitted grid system needs to be generated for the modified inlet/sting geometry after every boundary-layer update. The remeshing is inexpensively performed by displacing the grid points along the Y grid lines, which are in the nearly normal direction close to the body.

In the second approach, the body surface is selected to serve as a boundary for both the inviscid and the viscous algorithms. The no-slip condition is enforced at this boundary for the viscous problem. The viscous effects are transmitted to the inviscid flowfield via a prescribed mass flux distribution across the body surface. The new surface pressure distribution is interpreted as the response of the inviscid flowfield, and it is passed to the boundary layer for a subsequent update.

It remains now to define the flux distribution across the body surface. The normal velocity across the surface is related to the displacement thickness according to

$$V_{bl} = \frac{1}{\rho_e} \frac{\partial}{\partial s} (\rho_e u_e \delta^*) \tag{13}$$

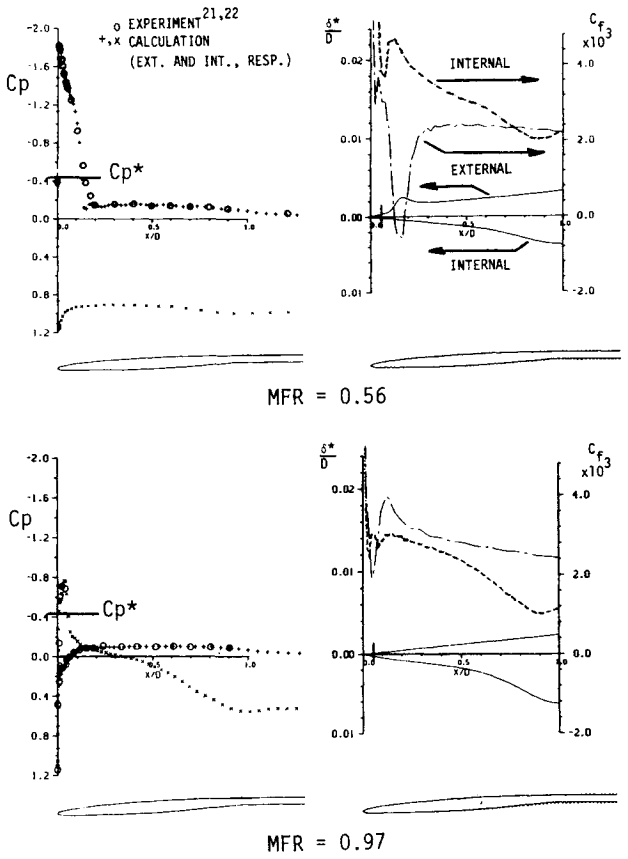

Fig. 2 **Pressure, displacement thickness, and skin-friction distributions for the NACA 1-85-100 inlet at $M_\infty = 0.8$ and $\alpha = 0°$.**

and it is used to determine the boundary condition in the inviscid flow solver

$$V_{bl} = \nabla\phi \cdot \boldsymbol{n} \tag{14}$$

Here, u_e is the velocity at the edge of the boundary layer and the differentiation $\partial/\partial s$ is done along the X family of grid lines, which is assumed to be approximately aligned with the streamlines. The unit vector normal to the surface

$$\boldsymbol{n} = (\boldsymbol{a}_1 \times \boldsymbol{a}_2)/|\boldsymbol{a}_1 \times \boldsymbol{a}_2| \tag{15}$$

is expressed in terms of the vectors along the X and Z mesh lines at the surface

$$\begin{vmatrix} \boldsymbol{a}_1 \\ \boldsymbol{a}_2 \\ \boldsymbol{a}_3 \end{vmatrix} = H^T \boldsymbol{e} \tag{16}$$

where H is the Jacobian matrix and $\boldsymbol{e}$ is the unit vector in the x, y, z system. It can be verified that

$$V_{bl} = h \frac{V}{|\boldsymbol{a}_1 \times \boldsymbol{a}_2|} \tag{17}$$

and the contravariant flux can be prescribed at the boundary.

Computational Aspects

Most of the calculations were performed on grids having $96 \times 24 \times 8$ cells in the X, Y, and Z directions, respectively. Additional cells in the circumferential direction do not affect the solutions appreciably for the flow cases considered here.

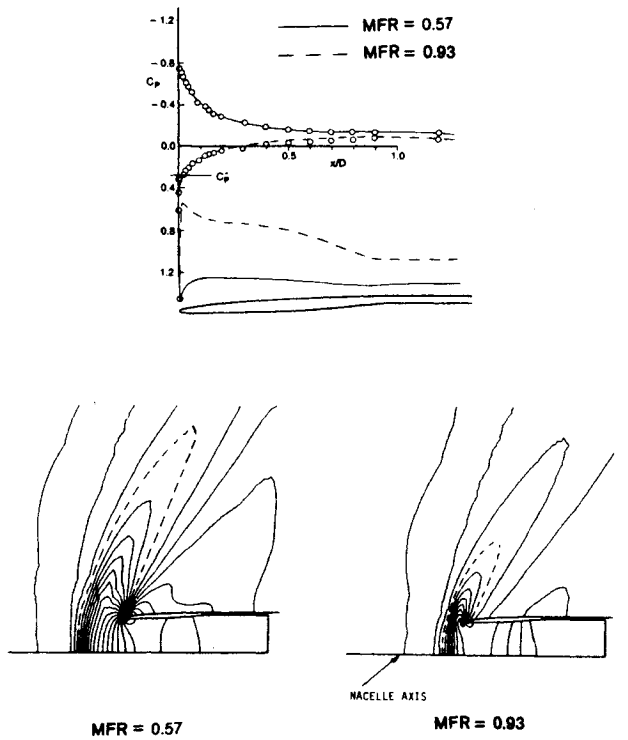

Fig. 3 **Pressure distributions and Mach number contours for the flow past the NACA 1-85-100 nacelle at $M_\infty = 1.2$ and $\alpha = 0°$.**

The multigrid procedure employs three grid levels.

The boundary-layer algorithm uses 61 points for each strip on either surface of the inlet, with high concentration of points near the stagnation region. Denser point distribution is also introduced in the vicinity of shocks for resolving the fine details of the flow in the shock/boundary-layer interaction zone.

The inviscid flow and the viscous flow calculations are performed intermittently until convergence is reached. The evolution of various quantities in the course of the iterative process is used to assess the convergence properties of the numerical scheme. These are the average residuals, the displacement thickness, the number of supersonic points detected in the flowfield, and the lift and drag forces. The inviscid flow solver usually requires eight work units (one work unit being defined as the labor required for a fine-grid sweep) for every visit to the boundary-layer module. Well-converged solutions are obtained in three or five viscous iterations. For flows with large separation bubbles, the boundary-layer update is done every 25 work units, requiring about 10 viscous iterations. For cases with sizeable separation zones, the calculations require computational time equivalent to approximately 50 CPU seconds on the CRAY XMP computer.

Results

Several inlets were used to exercise the capability of the present method to predict the flow for a wide spectrum of inlet operational conditions.

NACA 1-85-100 (1.046) Inlet

A series of solutions was obtained for an inlet that is operational at nearly sonic velocities. The first calculations are presented for the freestream Mach number of 0.8 and mass flow ratios (MFR) of 0.56 and 0.97. The experimental data[21,22] and the calculated pressure distributions are displayed in Fig. 2 (x/D being the distance in terms of inlet maximum diameter). These flow conditions demonstrate the profound effect the mass flow ratio has upon the local flow incidence. As the intake velocity decreases, the effective flow incidence in the

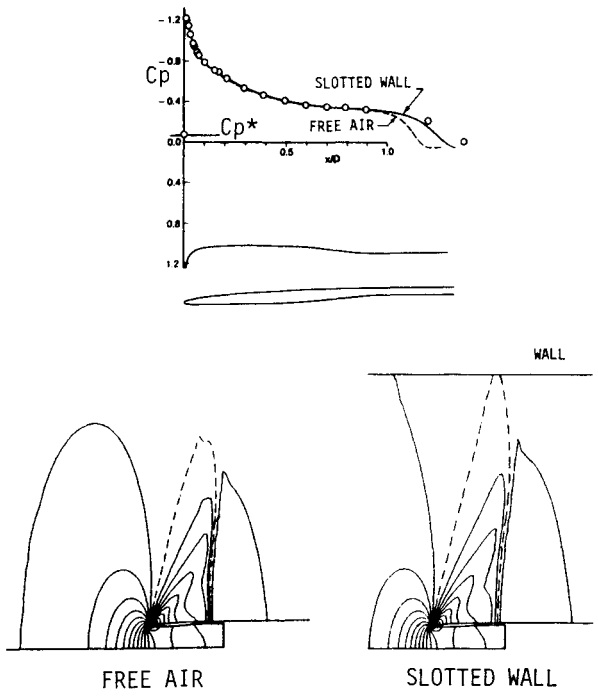

Fig. 4 Effect of wind-tunnel wall condition on the pressure distribution and Mach number maps for the NACA 1-85-100 nacelle at $M_\infty = 0.96$, $\alpha = 0°$, and $MFR = 0.56$.

highlight region becomes larger and the stagnation point moves inside the duct. As a result, a suction region develops on the external surface. Good agreement with the experimental prevails on both inlet surfaces, and minor discrepancies are noticeable downstream of the abrupt recompression in the low-mass flow ratio case. Notice the existence of a tiny supersonic bubble on the internal surface just aft of the highlight station for the high-*MFR* condition. The figure also presents the computed displacement thickness δ^* and skin-friction coefficient C_f for a Reynolds number of 5×10^6 (based on inlet maximum diameter). The transition locations on the external and internal surfaces are marked in the figure with the long vertical tick lines on the respective sides of the abscissa. In the low-*MFR* case, the calculation indicated local boundary-layer separation due to the steep pressure gradient across the shock.

In order to assess the capability of the code for computing low-supersonic freestream conditions, calculations for $M_\infty = 1.2$ for mass flow ratios of 0.57 and 0.93 were performed. The pressure distributions and Mach number contours are presented in Fig. 3. Throughout this paper the Mach number charts use increments of 0.05 and the dashed contour line represents $M = 1$. The computed results conform well with the experimental data. The salient feature of this supersonic flow condition is the formation of a bow shock upstream of the nacelle; this is the necessary mechanism for adjusting the mass flux inside the inlet. Notice that for large-intake *MFR*, less spillage is necessary to accommodate the fan face velocity, and consequently, the bow shock forms nearer to the nacelle.

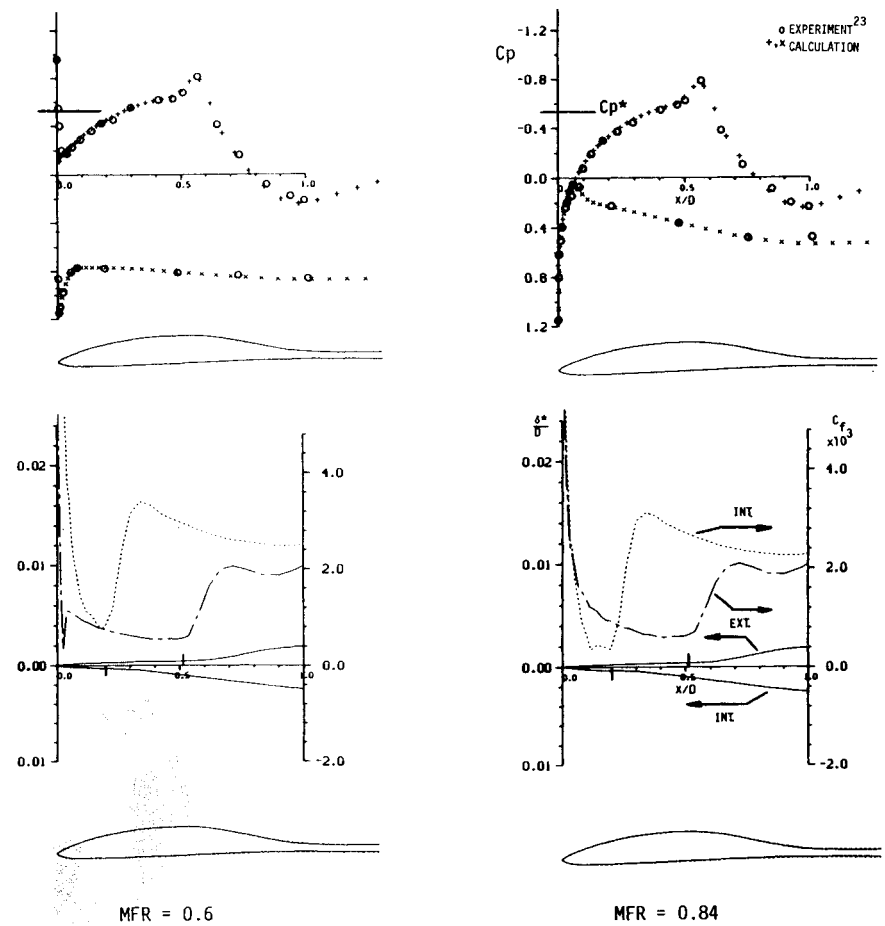

Fig. 5 Pressure distributions and boundary-layer characteristics for the G. E. natural laminar flow nacelle at $M_\infty = 0.775$ and $\alpha = 0°$.

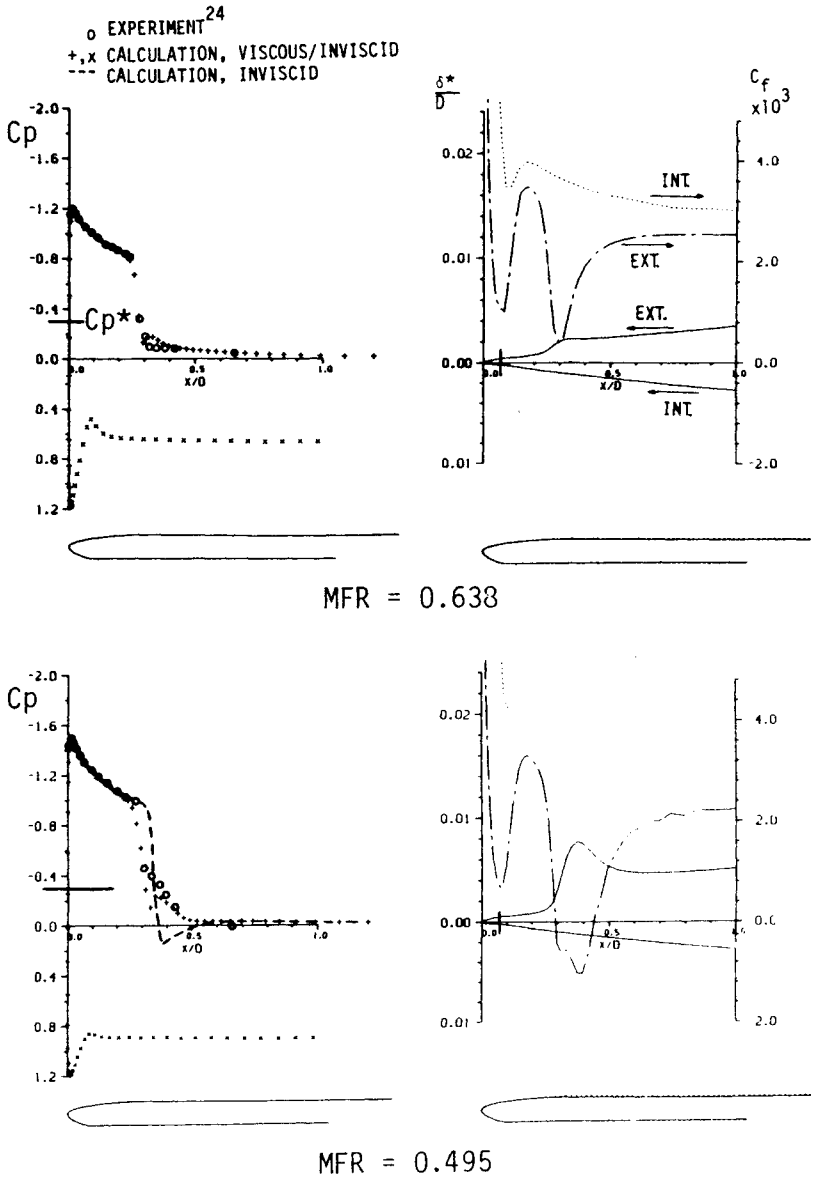

Fig. 6 Pressure distributions and boundary-layer properties for the inlet tested in Ref. 24 at $M_\infty = 0.85$ and $\alpha = 0°$.

To illustrate the importance of implementing wind-tunnel wall conditions consistent with the test facility, consider the freestream Mach number of 0.96 and $MFR = 0.56$. The computed pressure distributions and Mach number chart for the inlet in free air and the experimental C_p are shown in Fig. 4. The flow is predominantly supersonic on the external surface of the cowl. The agreement with the experimental data is good, except that the calculation predicts recompression at about the 1.1 diameter station, which is approximately 0.2 diameters upstream of the observed location. In an attempt to account for this difference, the program was modified to model the 4% slotted walls (for which $F = 0.712$) of the 16-ft (4.9-m) NASA Langley transonic tunnel used in the experiment. The results thus obtained are also presented in Fig. 4. The shock location is still slightly upstream of the experimentally observed location, but nevertheless, a significant part of the original discrepancy is accounted for. Although the height-to-diameter ratio for this particular arrangement is 10.61, for freestream Mach numbers close to sonic velocities, waves originating at the body surface propagate in the near vertical direction, and the supersonic pocket spans the tunnel. Not surprisingly, wall interference comes into play, and this is reflected in the computed C_p distributions.

General Electric Natural Laminar Flow Nacelle

The transonic flow past a natural laminar flow nacelle was investigated, and results are compared with the data reported in Ref. 23. The distributions of the pressure, displacement thickness, and skin-friction coefficient for $M_\infty = 0.775$ and $Re = 6.7 \times 10^6$ are shown in Fig. 5, indicating good agreement for the mass flux ratios considered. The nacelle is designed to achieve a favorable pressure distribution over its foreportion so that transition is delayed until the recompression. The transition locations were input at 0.52 and 0.2 stations on the external and internal surfaces, respectively. The aft transition location on the external surface results in reduced friction drag characteristics. It is noteworthy that the program predicts well the suction pressure spikes at the leading edge for $MFR = 0.6$ and that the flow is nearly separated in the laminar region for the low MFR. The calculations indicate that the flow is laminar until about the 50% diameter station, where δ^* is about 0.4 thousandths the diameter for all $MFRs$.

ARA Cowl # 5

Comparisons of computed results with the experimental data reported in Ref. 24 for a nacelle potentially applicable to the proposed superfan-engined aircraft are shown in Fig. 6 for

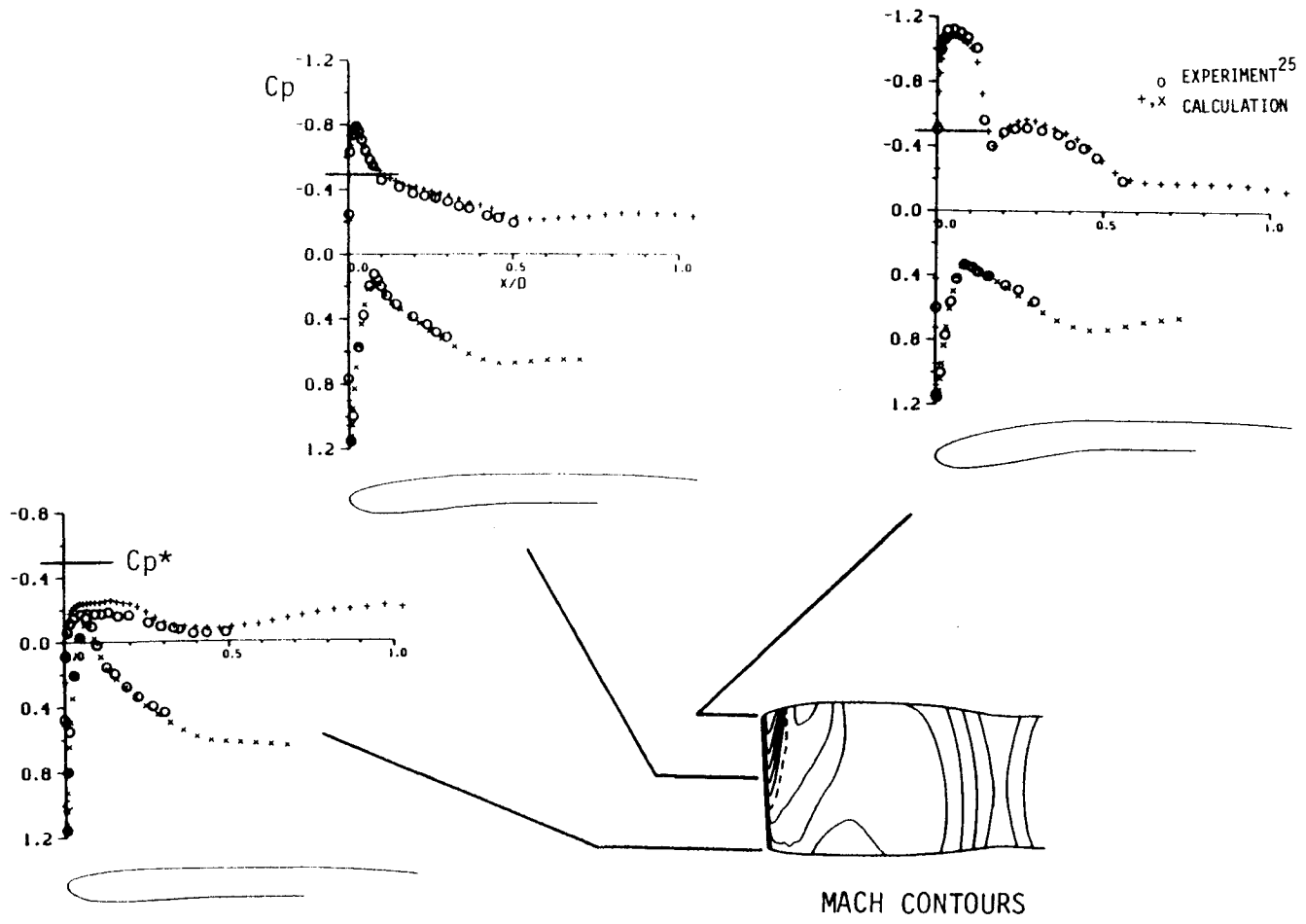

Fig. 7 Pressure distribution for the DC-10 inlet at $M_\infty = 0.78$, $\alpha = 8°$, and $MFR = 0.71$.

$M_\infty = 0.85$ and $Re = 2.4 \times 10^6$ at two mass flow settings. This figure also shows boundary layer growth and the associated skin-friction distribution. For $MFR = 0.638$, acceptable agreement prevails. Minor differences are confined to a small region at the foot of the shock. The C_f distribution on the external surface indicates that the flow at the shock is on the verge of separation. As the MFR decreases, the effective flow incidence becomes larger, resulting in the acceleration of the flow. As a consequence, the shock becomes stronger and the boundary layer can no longer negotiate the adverse pressure gradient. A separation bubble that extends over a 0.15-diameter zone is formed. Differences between computed and experimental C_p distributions are noted in that region. The importance of including viscous effects in the prediction of complex shock/boundary-layer interacting flows is evident in the companion figure in which the result for the inviscid calculation is shown. The inviscid-viscous calculation places the shock at the right location, and pressure levels downstream of the shock are greatly improved.

DC-10-Type Inlet

Calculations were perfomed for the nacelle, which is mounted on wide-body transports like the McDonnell Douglas DC-10. The pressure distributions at the leeward, transverse, and windward sections for $M_\infty = 0.78$, $MFR = 0.71$, and $Re = 3.7 \times 10^6$ at an 8 deg angle of attack are shown in Fig. 7 together with the experimental data.[25] At these conditions, a shock exists on the external surface. It is the strongest at the leeward section, and its strength subsides toward the transverse section. In fact, at the windward section, the shock ceases to exist. This can also be inferred from the Mach number contours.

Although good agreement with the experiment is obtained, the calculation underpredicts the pressure level on the external leeward surface and overpredicts it at the windward side. This is possibly because the inlet has lift. The true angle of attack was somewhat higher than the measured value due to the deflection of the sting upon which the nacelle was mounted. The sting deflection was not accounted for in the data reduction. This contention is supported by the fact that the discrepancy is not observed for cases in which the lift is near zero.

Next, consider the freestream having a 0.84 Mach number. The Reynolds number is 3.6 million, and MFR is set to 0.83. The solution for a 0 deg angle of attack is shown in Fig. 8. The comparison with the experimental Cp is shown in Fig. 8a. The agreement with the inviscid/viscous solution is good. For this high-freestream Mach number, a large portion of the inlet surface is immersed in supersonic flow. In particular, a strong shock develops at the rear of the supersonic bubble inside the inlet. Figure 8a also shows the inviscid solution obtained with the program. Notice that inclusion of the viscous effects is important for predicting more realistic flowfields. The viscous/inviscid procedure places the shocks at the right locations and predicts the shock strengths much more precisely.

Figure 8b presents the predicted boundary-layer characteristics. It is shown that the boundary-layer thickness grows quite abruptly right downstream of the shock in the diffuser at the leeward section. A separation bubble is triggered as indicated by the contours of the skin-friction coefficient on the internal surface in the region where it becomes negative. Figure 8c presents surface contours of the flow characteristics.

Figure 8d presents the Mach number map on the vertical plane of symmetry, showing the extent of the supersonic pocket. The plot shows that a doughnut-shaped supersonic bubble sits on both surfaces of the inlet.

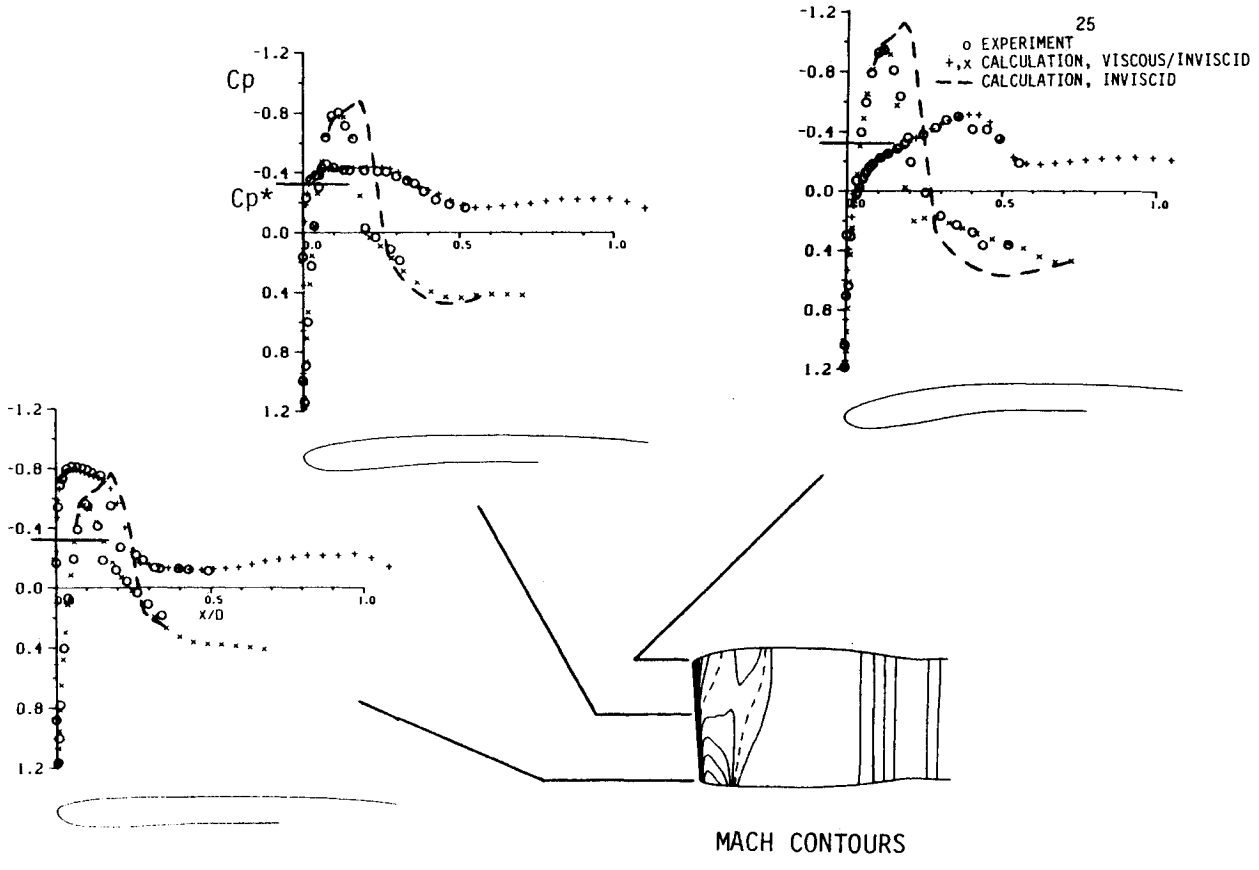

Fig. 8a Pressure distribution for the DC-10 nacelle at $M_\infty = 0.84$, $\alpha = 0°$, and $MFR = 0.83$.

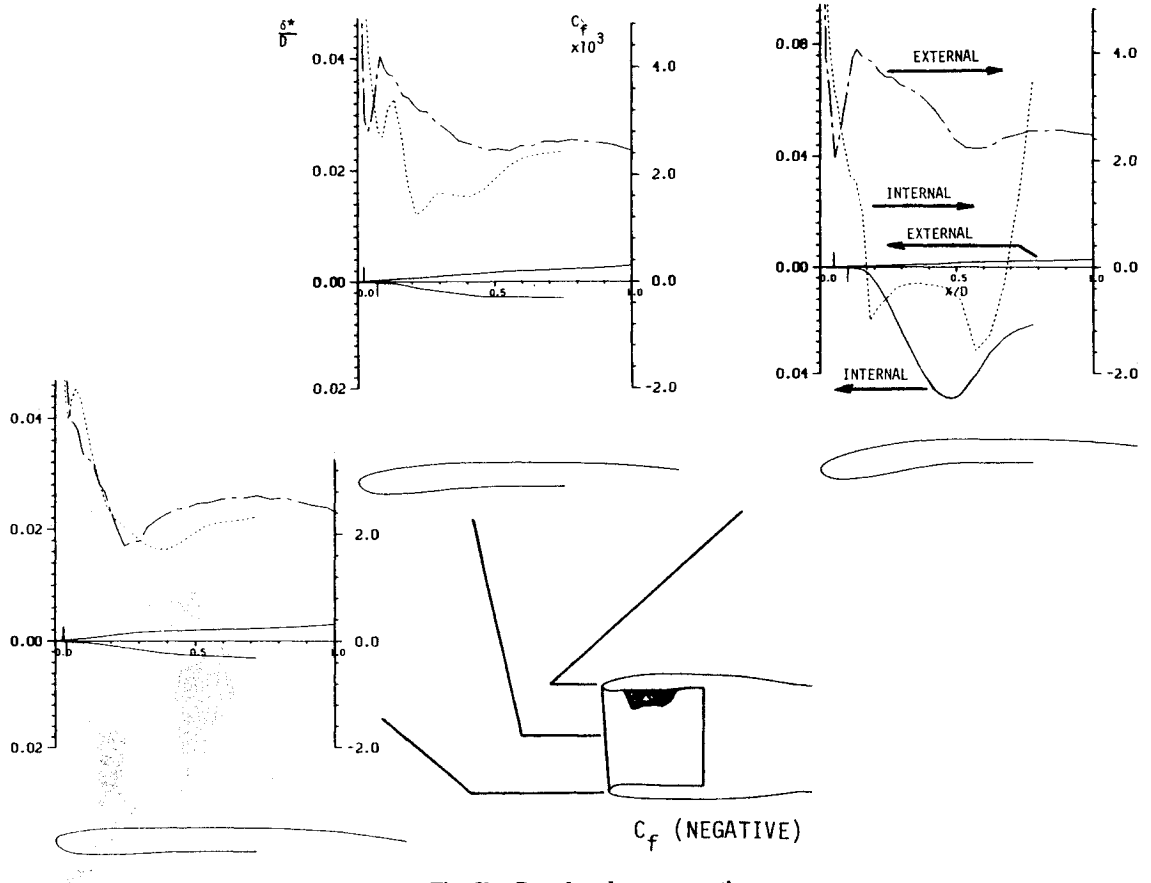

Fig. 8b Boundary-layer properties.

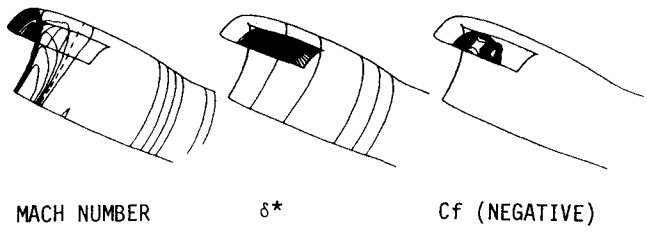

Fig. 8c Flow characteristics on the inlet surface.

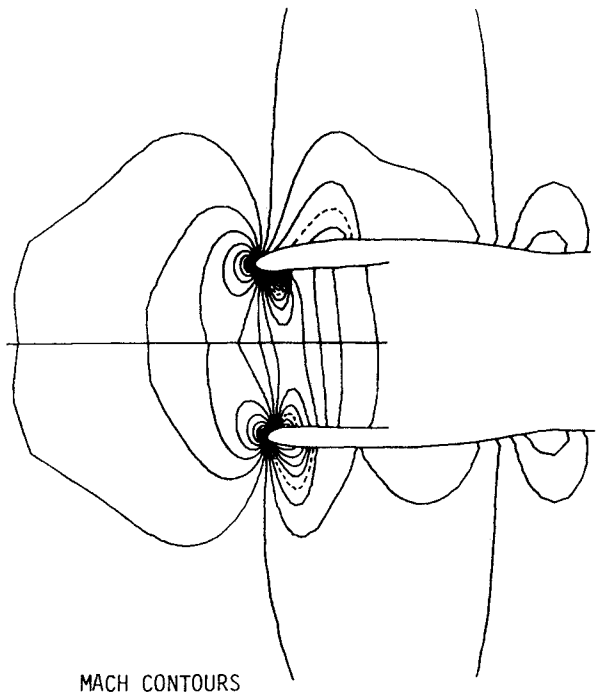

Fig. 8d Mach number contours on the vertical plane of symmetry.

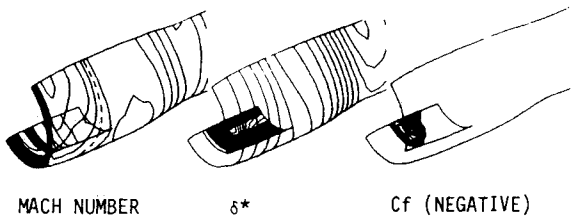

Fig. 9 Flow characteristics on the DC-10 inlet at $\alpha = 8°$, M_∞, and *MFR* as in Fig. 8.

As the flow incidence increases, the internal shock dwindles at the leeward side and its intensity is amplified at the windward section. At an 8 deg angle of attack, a separation bubble forms at the windward side. This flow situation is presented in Fig. 9.

Conclusion

A computational method for calculating transonic flowfields about arbitrary inlets at incidence has been developed. The method uses the potential finite-volume multigrid tecnique in conjunction with a finite-difference boundary-layer procedure in an interactive mode. The boundary-layer problem is formulated in the inverse mode in order to ensure stability of calculations for flowfields containing separation bubbles. The test of merit of the present approach lies in its reliability in providing insight into the nature of the flow pattern associated with shock-induced separated flowfields with reasonable expenditure of computer resources.

References

[1]Arlinger, B. G., "Calculation of Transonic Flow Around Axisymmetric Inlets," *AIAA Journal*, Vol. 13, Dec. 1975, pp. 1614–1621.

[2]Caughey, D. A. and Jameson, A., "Accelerated Iterative Calculation of Transonic Nacelle Flowfields," AIAA Paper 76–100, 1976.

[3]Reyhner, T. A., "Computation of Transonic Potential Flow About Three-Dimensional Inlets, Ducts and Bodies," NASA CR–3514, 1982.

[4]Chen, L. T. and Caughey, D. A., "Higher-Order, Finite-Difference Scheme for Three-Dimensional Transonic Flowfields About Axisymmetric Bodies," *Journal of Aircraft*, Vol. 17, Sept. 1980, pp. 668–676.

[5]Deese, J. E. and Agarwal, R. K., "Calculation of Axisymmetric Inlet Flowfield Using the Euler Equations," AIAA Paper 83–1853, 1983.

[6]Bush, R. H., "External Compression Inlet Predictions Using an Implicit Upwind, Multiple Zone Approach," *Proceedings of the AIAA 7th Computational Fluid Dynamics Conference*, 1985.

[7]Vadyak, J., "Simulation of Transonic Three-Dimensional Nacelle/Inlet Flowfields Using an Euler/Navier-Stokes Algorithm," AIAA Paper 85–0084, 1985.

[8]Jameson, A. and Caughey, D. A., "A Finite-Volume Method for Transonic Potential Flow Calculations," *Proceedings of the AIAA 3rd Computational Fluid Dynamics Conference*, 1977.

[9]Halsey, N. D., "Conformal Mapping as an Aid in Grid Generation for Complex Three-Dimensional Configurations," AIAA Paper 86–0497, 1986.

[10]Shmilovich, A. and Caughey, D. A., "Application of the Multigrid Method to Calculations of Transonic Potential Flow About Wing-Fuselage Combinations," *Journal of Computational Physics*, Vol. 48, Dec. 1982, pp. 462–484.

[11]Caughey, D. A. and Shmilovich, A., "Multigrid Calculation of Transonic Potential Flows," *Numerical Methods in Fluids: Advances in Computational Transonics*, Vol. 4, edited by W. W. Habashi, Pineridge Press, Swansea, UK, 1983.

[12]Shmilovich, A. and Caughey, D. A., "Calculation of Transonic Potential Flow Past Wing-Tail-Fuselage Configurations Using the Multigrid Technique," *Lecture Notes in Physics*, Vol. 218, Springer-Verlag, Berlin, 1984, also *Journal of Aircraft*, Vol. 22, July 1985, pp. 581–586.

[13]Cebeci, T., "Separated Flows and Their Representation by Boundary-Layer Equations," Mechanical Engineering Rept. ONR–CR215–234–2, California State University, Long Beach, CA, 1976.

[14]Cebeci, T., Chen, L. T., and Chang, K. C., "An Interactive Scheme for Three-Dimensional Transonic Flows," *Numerical and Physical Aspects of Aerodynamic Flows III*, edited by T. Cebeci, Springer-Verlag, New York, 1986.

[15]Shmilovich, A., "Programs for Calculation of Transonic Flow Past Inlets," DACTRAN-32, -31 and -31Y, McDonnell Douglas Rept. K0446, 1987.

[16]Laynaert, J., Transonic Testing of the Engine Nacelle Air Intake and Afterbody," NASA TT F-14, 154, March 1972.

[17]Shmilovich, A. and Caughey, D. A., "On Transonic Flow Computations About Airfoils and Bodies of Revolution in Free Air and in Wind Tunnels," *Proceedings of the 11th World Congress of the International Association of Mathematical and Computational Simulation*, Oslo, Norway Vol. 2, North-Holland Publishing, Aug. 1985, pp. 109–112.

[18]Cebeci, T. and Smith, A. M. O., *Analysis of Turbulent Boundary Layers*, Academic, New York, 1974.

[19]Bradshaw, P., Cebeci, T., and Whitelaw, J. H., *Engineering Calculation Methods for Turbulent Flow*, Academic, London, 1981.

[20]Reyhner, T. A. and Flügge-Lotz, I., "The Interaction of a Shock Wave with a Laminar Boundary Layer," *International Journal of Non-Linear Mechanics*, Vol. 3, June 1968, pp. 173–199.

[21]Re, J. R., "An Investigation of Several NACA 1-Series Axisymmetric Inlets at Mach numbers from 0.4 to 1.29," NASA TM X-2917, 1974.

[22]Re, J. R., "An Investigation of Several NACA 1-Series Inlets at Mach Numbers from 0.4 to 1.29 for Mass-Flow Ratios Near 1.0," NASA TM X-3324, 1974.

[23]Younghans, J. L. and Lahti, D. J., "Experimental Studies on Natural Laminar Flow Nacelles," AIAA Paper 84–0034, 1984.

[24]Langley, M. J., "The Design of Axisymmetric Cowls for Podded Nacelles for High By-Pass Ratio Turbofan Engines, Aircraft Research Association R&M 3846, 1979.

[25]Private communication, 1985.